IEEE Access
Multidisciplinary | Rapid Review | Open Access Journal

Received March 28, 2022, accepted April 10, 2022, date of publication April 14, 2022, date of current version April 25, 2022.

*Digital Object Identifier 10.1109/ACCESS.2022.3167437*

# 3-D Printed Plug and Play Prototyping for Low-Cost Sub-THz Subsystems

**SANG-HEE SHIN[1], (Member, IEEE), ROSHAN PAYAPULLI[1], LIYAN ZHU[1], MANOJ STANLEY[2], (Member, IEEE), XIAOBANG SHANG[2], (Senior Member, IEEE), NICK M. RIDLER[2], (Fellow, IEEE), AND STEPAN LUCYSZYN[1], (Fellow, IEEE)**

[1]Department of Electrical and Electronic Engineering, Imperial College London, London SW7 2AZ, U.K.
[2]Department of Electromagnetic and Electrochemical Technologies, National Physical Laboratory, Teddington TW11 0LW, U.K.

Corresponding author: Stepan Lucyszyn (s.lucyszyn@imperial.ac.uk)

This work was supported by the U.K. Space Agency's Centre for Earth Observation Instrumentation (CEOI) under Grant RP10G0435A202.

**ABSTRACT** Polymer-based additive manufacturing using 3-D printing for upper-millimeter-wave (*ca.* 100 to 300 GHz) frequency applications is now emerging. Building on our previous work, with metal-pipe rectangular waveguides and free-space quasi-optical components, this paper brings the two media together at G-band (140 to 220 GHz), by demonstrating a compact multi-channel front-end subsystem. Here, the proof-of-concept demonstrator integrates eight different types of 3-D printed components (30 individual components in total). In addition, the housing for two test platforms and the subsystem are all 3-D printed as single pieces, to support plug and play development; offering effortless component assembly and alignment. We introduce bespoke free-space TRM calibration and measurement schemes with our quasi-optical test platforms. Equal power splitting plays a critical role in our multi-channel application. Here, we introduce a broadband 3-D printed quasi-optical beamsplitter for upper-millimeter-wave applications. Our quantitative and/or qualitative performance evaluations for individual components and the complete integrated subsystem, demonstrate the potential for using consumer-level desktop 3-D printing technologies at such high frequencies. This work opens-up new opportunities for low-cost, rapid prototyping and small-batch production of complete millimeter-wave front-end subsystems.

**INDEX TERMS** Additive manufacturing, 3-D printing, millimeter-wave, sub-THz, G-band, WR-5, WM-1295, quasi-optics, dielectric lens, beamsplitter.

## I. INTRODUCTION

Over the past few years, companies have been adopting additive manufacturing techniques as a standard means of rapid prototyping and small-batch production. For example, 3-D printing has inherent advantages with fast turn-around, weight reduction (employing unique topological solutions) and waste reduction, when compared to subtractive manufacturing. These significant advantages already play a key role within the aerospace and high-performance automotive industries.

Polymer-based 3-D printing is now showing great potential for the rapid prototyping of passive components and circuits for microwave-to-terahertz (THz) applications. For example, Timbie *et al.* demonstrated a 3-D printed metal-pipe rectangular waveguide (MPRWG) and corrugated horn antenna at W-band (75 to 110 GHz) [1]. Three years later, Bieren *et al.* reported a MPRWG and diagonal horn antenna at WR-3.4 band (220 to 330 GHz) [2]. The following year, we reported our detailed investigation for implementing high performance 3-D printed MPRWGs; covering both X-band (8 to 12 GHz) and W-band, while also demonstrating a high performance E-plane split-block iris-coupled 6$^{th}$ order band-pass filter (BPF) at W-band [3]. Since then, we have moved 3-D printed MPRWGs up in frequency; covering the WM-380 band (500 to 750 GHz) and WM-250 band (750 GHz to 1.1 THz) [4].

These early works [1]–[4] are non-reconfigurable, in the sense that the reported components are neither mechanically or electrically tunable. In order to expand the functionality for 3-D printing, in addition to metal-plated structures, we have accurately characterized important polymer-based

The associate editor coordinating the review of this manuscript and approving it for publication was Xi Zhu.

building materials. For example, a relatively low loss acrylonitrile butadiene styrene (ABS) material was characterized over X-band [5] and Ku-band (12 to 18 GHz) [6]. This build material was then employed in mechanically-tunable 3-D printed dielectric-insert phase shifters at both X-band [7] and Ku-band [8]. In addition, carbon-loaded conductive polylactic acid (PLA) was also characterized across both X- and Ku-bands [6]. This build material was then employed in a mechanically-tunable rotary vane attenuator at Ku-band [6].

While mechanically-tunable 3-D printed components are interesting, there are still reliability issues. For this reason, the first passive-active hybrid technology was demonstrated, having 3-D printed waveguide flanges, delay lines and power splitters/combiners and, more significantly, with integrated high-resistivity silicon implants and laser diodes; creating an electronically-tunable I-Q vector modulator at WR-2.2 band (325 to 500 GHz) [9].

Integrating multiple 3-D printed components together offers the important advantage of removing impedance mismatch losses between flanges. For example, both Rohrdantz *et al.* [10] and later Dimitriadis *et al.* [11], demonstrated a non-tunable 4-element antenna array at Ka-band (26.5 to 40 GHz). In contrast, our group recently demonstrated a mechanically-tunable 3-D printed beam-steerable 4-element phased-array antenna at Ku-band [8].

In addition to the advances being demonstrated with integrated waveguide-based subsystems, Harris Corp. (USA) recently reported two commercial (conventionally-machined) open-ended waveguides that are coupled via a pair of 3-D printed lens, using an in-line alignment frame at lower millimeter-wave frequencies (*ca.* 30 to 100 GHz) [12], [13]. In 2021, we reported our detailed investigation for implementing high performance 3-D printed quasi-optical components (rectangular horn antenna, off-axis parabolic mirror (OAPM), convex and Fresnel lenses, polarizer, radiation absorbent material (RAM) and a reconfigurable 'plug and play' housing for undertaking the free-space characterization of these components) at G-band (140 to 220 GHz) [14].

An exhaustive survey of polymer-based 3-D printed microwave-to-THz applications has not been given here, as most of the relevant articles have already been cited in our previous papers.

This paper significantly advances 3-D printing by fully integrating both waveguide and quasi-optical components, to create a compact multi-channel subsystem proof-of-concept demonstrator. Here, the proposed front-end sub-THz subsystem integrates 30 individual components: 1× OAPM, 1× plano-concave lens, 1× reconfigurable flat mirror, 5× flat mirrors, 4× beamsplitters, 6× plano-convex lenses, 6× horn antennas and 6× BPFs. Only the OAPM and horn antennas were previously reported [14], while the plano-convex lens has been redesigned for this new bespoke application. As a result, details of their design, fabrication and characterization can be found in [14]. This work introduces our concave lens and flat mirrors, while concentrating on a novel broadband beamsplitter; requiring custom 3-D printed test platforms.

More importantly, this paper demonstrates the proof-of-concept for a fully 3-D printed integrated plug and play prototype architecture. This paper will show the effectiveness of 3-D printing for achieving good alignment, without the need for a skilled operator to use costly optical aligners for individual components (normally taking many hours). Potential subsystem applications include low-cost millimeter-wave metrology, aerospace radiometer and communications payloads, as well as front-ends for +5G base stations.

## II. DESIGN

Our design goal is to implement a compact front-end subsystem architecture (with details given in Subsection D). In this section, we describe the design of the bespoke prototype dielectric lenses, holey beamsplitter and also the test platforms and subsystem housings. From the outset, it was decided that the complete single-piece subsystem housing would fit within the maximum build volume (280 mm × 350 mm × 300 mm) of our fused deposition modelling (FDM) 3-D printer (Raise Pro 2). Multiple housing parts would compromise alignment accuracy and structural integrity.

### A. DIELECTRIC LENSES

The compact nature of our architecture dictates a number of design implantation choices. For example, lenses are chosen over mirrors to focus and collimate beams, minimizing signal path complexity; this also allows a significant reduction in both volume and mass, but increases transmission losses (discussed in Section VI).

Two different types of hyperbolic aspherical lenses are designed for the subsystem: a plano-convex lens [14] and a plano-concave lens.

The main input test beam is externally collimated by a commercial antenna-OAPM pair [14]. With the OAPM, the two-sigma (i.e., $1/e^2$ normalized power) boundary for the collimated Gaussian beam (containing approximately 95% of the beam power) projected into the subsystem's main input window has an estimated $1/e^2$ beamwidth that is less than 50 mm (i.e., below the 76.2 mm diameter of the OAPMs, to minimize diffraction losses with both the external commercial OAPM and its internal 3-D printed OAPM replica [14]).

The internal beamwidth is significantly reduced to approximately 20 mm, to reduce the width of the lenses (helping to make the subsystem more compact) and, therefore, also reduces their thickness (lowering transmission losses with plano-convex lenses). At the output of the internal OAPM, a convex lens could have been chosen. However, in order to significantly reduce the transmission path length (to achieve a compact subsystem), a hyperbolic aspherical plano-concave lens is chosen. In addition, six hyperbolic aspherical plano-convex lenses are employed for our 6-channel architecture, each focusing the internal collimated beam into its corresponding channel output horn antenna.

The building material for the lenses is chosen to be the Elegoo Water Washable Rapid Resin (Ceramic Grey), as its

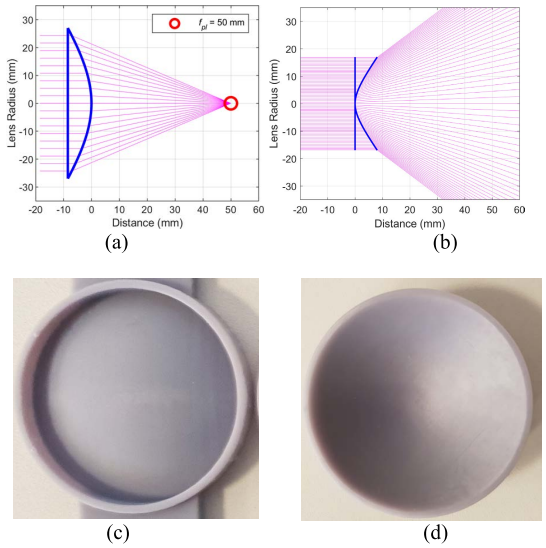


**FIGURE 1.** 3-D printed lenses: (a) simple ray tracing for the plano-convex lens; (b) simple ray tracing for the plano-concave lens; (c) photograph of the plano-convex lens; and (d) photograph of the plano-concave lens.

**TABLE 1.** Design properties for the dielectric lenses.

| Property | Plano-convex | Plano-concave |
|---|---|---|
| Center Thickness (mm) | 4.589 | 1.000 |
| Edge Thickness (mm) | 10.00 | 9.070 |
| Diameter (mm) | 35.00 | 33.91 |
| Rim Width (mm) | 1.250 | 1.000 |
| Material | Elegoo Water Washable Gray | |
| Refractive Index [14] | 1.7 (G-band) | |

dielectric properties are already characterized from our previous work [14]: dielectric constant $\varepsilon_r \approx 2.89$ and loss tangent $tan\delta \approx 0.032$ across G-band. The hyperbolic aspherical curvatures for both plano-concave and plano-convex lenses, use the following design equation [14]:

$$z^2(r)\,(\varepsilon_r - 1) + 2f_{pl}z(r)\left(\sqrt{\varepsilon_r} - 1\right) - r^2 = 0 \qquad (1)$$

where $f_{pl}$ is the target focal path length, $z(r)$ is the curvature profile and $r$ is the corresponding radial distance. Also, to verify the design, a custom MATLAB code is written for optical ray-tracing, with results shown in Fig. 1(a). It can be seen that the plano-convex lens design can provide a perfect optical focus with the target focal path length of $f_{pl} = 50$ mm. Figure 1(b) shows that the plano-concave lens is able to collimate a converging beam. In both cases, spherical aberration is not theoretically present. In practice, however, because the input source cannot be perfectly collimated, the lenses will not be able to focus/collimate perfectly. 3-D printed lenses and the key properties of the lenses are shown on Fig. 1 and Table 1, respectively.

### B. HOLEY BEAMSPLITTER

To split an incident collimated beam into two separate beams of equal power, a holey beamsplitter is developed for this application. Conventional wideband free-space beam

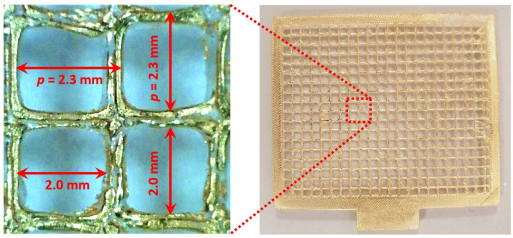


**FIGURE 2.** 3-D printed and gold-leaf gilded holey beamsplitter: (left) zoomed-in photograph; and (right) photograph of the complete component.

splitting is commonly achieved using a 'polka dot beamsplitter' at optical frequencies (infrared and visible) [15], [16]. The polka dot beamsplitter consists of a 2-D periodic array of metalized patches (typically circular or square) that masks 50% of its glass substrate. Because the size of each patch is sufficiently larger than the maximum in-band optical wavelength, it has an excellent performance over a wide bandwidth [17].

For (sub-)THz frequencies, sub-wavelength metasurface beamsplitters have been reported, based on either a 2-D or 3-D periodic array [18]–[22]. However, as the required minimum feature size for the patch is sub-100 $\mu$m, it is not possible to manufacture these beamsplitters for upper-millimeter-wave frequencies (*ca.* 100 to 300 GHz) using currently available desktop 3-D printers. Also, due to their sub-wavelength periodicity, they exhibit frequency dispersion and, therefore, narrow bandwidth.

Another low-cost approach for achieving free-space power splitting, at THz frequencies, employs an electrically thin-film metal-coated dielectric substrate. For example, a sub-skin depth layer of silver paint can be deposited onto a low-density polyethylene substrate [23].

Our holey beamsplitter design is inspired by the concept of the polka dot beamsplitter, by exploiting Babinet's principle to create the complementary structure (i.e., the metal patches are replaced by a metal mesh), which avoids the need for printing the non-metalized areas of the substrate. This solution allows the beamsplitter to be manufactured using conventional FDM 3-D printing and metal plated using gold leaf gilding techniques [14].

FDM 3-D printing has poor dimensional precision and print consistency for sub-millimeter minimum feature sizes. Moreover, a single layer of gold leaf (having a manufacturer's quoted thickness of 0.12 $\mu$m [14]) exhibits less than one skin depth across G-band (ranging from 0.167 to 0.210 $\mu$m); simulations for a single layer of gold leaf show that this is sufficient to provide a screening effectiveness [24] of approximately 59 dB and return loss of 0.01 dB, across G-band. A conventional approach for achieving equal transmittance and reflectance was not possible with a 50% metallized coverage area. Since we do not have the computational resource to undertake the necessary 3-D electromagnetic modelling, we adopted an iterative 'trial and error' design-manufacture-test cycle; fortunately, our solution lends itself to rapid

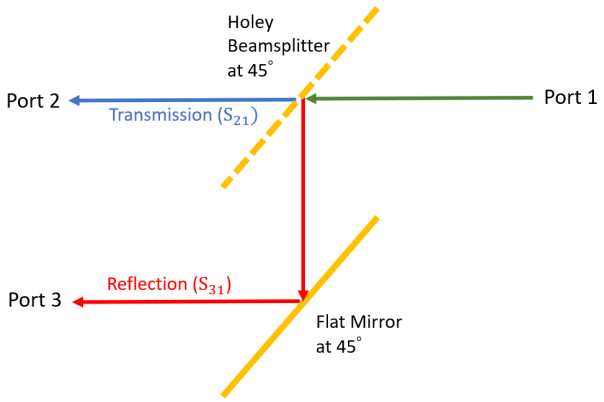


**FIGURE 3.** Illustration of beam paths for testing the holey beamsplitter.

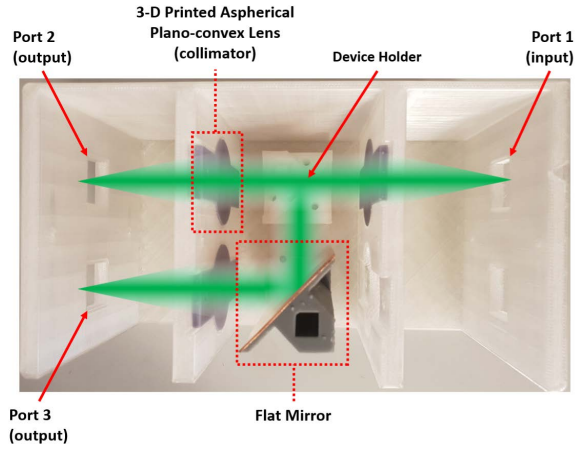


**FIGURE 4.** 3-D Printed reconfigurable quasi-optical 3-port test platform.

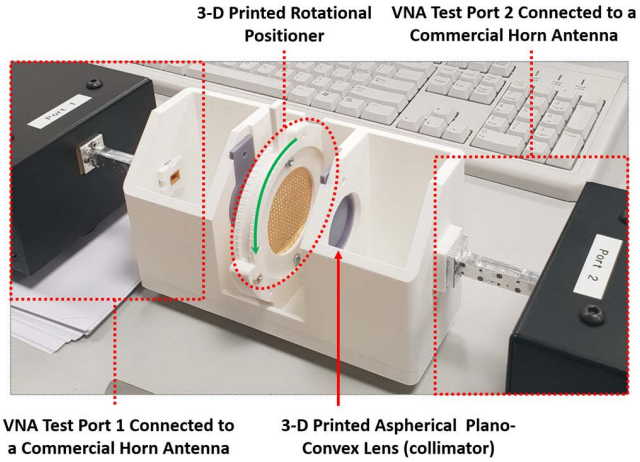


**FIGURE 5.** 3-D printed quasi-optical rotating test platform with holey beamsplitter as the device under test.

prototyping using 3-D printing. The key dimensions and photograph of the final version of our beamsplitter is shown in Fig. 2.

It is important to note that the beamsplitter's lattice constant $p = 2.3$ mm $\gg \lambda_{\max}(140\ \text{GHz})/10 = 0.2$ mm, which means it cannot be treated as a homogeneous subwavelength metasurface (which would otherwise require $p < \lambda/10$); as such, with $p \sim \lambda$, our beamsplitter design falls under the heading of quasi-optics (which excludes both simple electromagnetic theory and simple geometrical optics ray tracing).

The power transmittance ($\mathcal{T} = |S_{21}|^2$) and reflectance ($\mathcal{R} = |S_{31}|^2$) measurement setup is shown in Fig. 3. An ideal, lossless beamsplitter has $\mathcal{T} = \mathcal{R} = 0.5$, while our primary objective is just to achieve $\mathcal{T} = \mathcal{R}$ across G-band.

Absorptance ($A$), which includes all losses (e.g., scattering, diffraction, ohmic and non-ideal bean collimation), is represented by:

$$\mathcal{A} = 1 - |S_{11}|^2 - |S_{21}|^2 - |S_{31}|^2 \approx 1 - |S_{21}|^2 - |S_{31}|^2 \qquad (2)$$

With our 2-port measurements, the input return losses are $-10log\,|S_{11}|^2 < 20$ dB across more than 80% of G-band and so the simplifying approximation in (2) can be justified.

### C. TEST PLATFORMS

To test the 3-port holey beamsplitter, at its intended oblique incidence angle of 45°, two 2-port measurements are needed; with a common input port (Port 1) and two output ports (Port 2 and Port 3), as illustrated in Fig. 3. Both output ports need to face the input port, due to the limited cable lengths between the VNA and frequency extension heads, and also to avoid unnecessary movement of the cables [14]. To accommodate these requirements, a bespoke reconfigurable quasi-optical 3-port test platform is required. Our 3-D printed plug and play test platform has pre-aligned slots for the horn antennas (in their 3-D printed adapters) and collimating plano-convex lenses. The beams transmitted through and reflected by the beamsplitter are focused by plano-convex lens into the corresponding commercial horn antennas at Port 2 and Port 3, respectively; with the latter, a flat mirror is needed to redirect the beam and this should be positioned parallel to the beamsplitter. The 3-D printed 3-port test platform is shown in Fig. 4, without a device under test.

Our input and internal beams are all vertically polarized. To evaluate the beamsplitter's polarization response, a bespoke quasi-optical rotating test platform is 3-D printed and fitted with a rotational positioner (having 3-D printed alignment markers at every 5° intervals of rotation, over a 90° arc). Here, the intended incidence angle is fixed at 0°. The 3-D printed quasi-optical rotating test platform is shown in Fig. 5.

### D. SUBSYSTEM HOUSING

The complete single-piece subsystem housing is designed to have external dimensions of 279 mm × 265 mm × 92 mm, integrating 30 individual components. Our prototype architecture is designed to support multiple iterations on the development of each component. For this reason, our plug and play methodology employs pre-aligned snap-in brackets for each component.

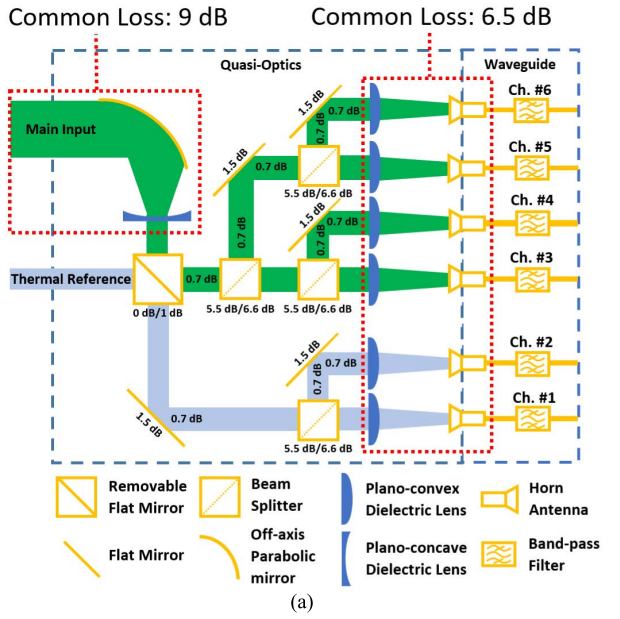


(a)

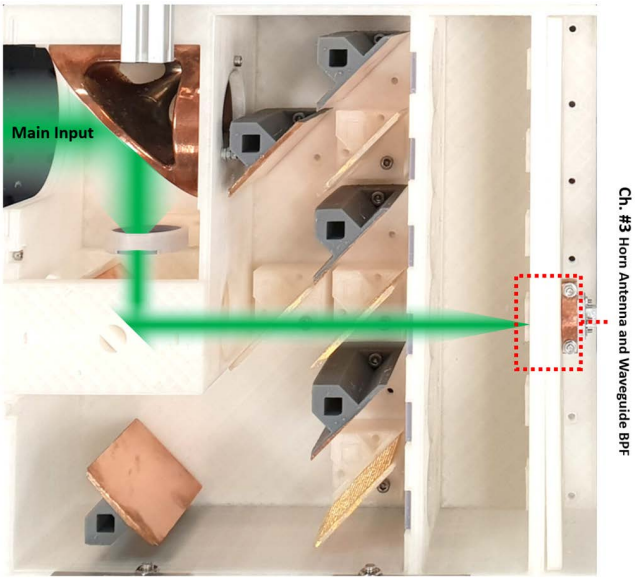


(b)

**FIGURE 6.** 3-D printed quasi-optical housing fitted with all 3-D printed components: (a) block diagram; and (b) photograph (plan view) with beam illustration for Ch. #3 measurement.

A block diagram for the compact multi-channel subsystem architecture is illustrated in Fig. 6(a), with associated beam paths for each of the six channels. In addition to the main input, an auxiliary window is included with the option for the subsystem channel receivers to 'see' external hot or cold reference sources. The removable flat mirror has two settings. When inserted, Channels #1 and #2 can 'see' the thermal reference sources (blue beams in Fig. 6(a)), while Channels #3 to #6 'see' the main input (green beams in Fig. 6(a)). In contrast, when removed, Channels #1 and #2 'see' the main input, while Channels #3 to #6 'see' the thermal reference sources. Although we changed the removable flat mirror settings manually (for convenience), our 3-D printed housing accommodates an electrically-actuated switching mechanism; this could then be used to implement a Dicke switch for radiometry applications.

The fully 3-D printed quasi-optical housing with integrated components for our proof-of-concept demonstration is shown in Fig. 6(b). When compared to using a commercially-machined breadboard and off-the-shelf optical components and their positioners, 3-D printing for prototyping of a complete front-end subsystem offers the important advantage of providing a much more compact solution. In addition, component assembly and alignment are effortless [14]. It can be seen in Fig. 6(b) that a near-optimal configuration is achieved in terms of size and compactness.

**TABLE 2.** Component 3-D printing and metallization implementation.

| Component | CAD Drawing | Slicer | Printer Technology | Printer Model | Metallization |
|---|---|---|---|---|---|
| Housings [14] | Autodesk Fusion 360 [25] | IdeaMaker [26] | FDM | Raise Pro 2 [27] | - |
| OAPM [14] | | PreForm [28] | SLA | Form 3 [29] | Copper Commercial Electroplating |
| Flat Mirrors | | | | | Copper Foil Lamination |
| Lens [14] | | Chitubox [30] | MSLA | Elegoo Mars 2 Pro [31] | - |
| Antennas [14] | | | | | Copper Commercial Electroplating |
| Filters | | | | | |
| Beamsplitter | OpenSCAD [32] | Simplify 3D [33] | FDM | Prusa MK3 [34] | Gold Leaf Gilding |

## III. FABRICATION

### A. 3-D PRINTING

Table 2 lists the various components, from the test platforms and subsystem housings to individual components, and their methods of implementation [14]. In general, each component has unique methods of implementation; the rationale for this has already been discussed in detail [14].

Details will now be given for the new components not previously reported. With the flat mirrors, to avoid the relatively high cost of commercial electroplating, a single sheet of $\sim$25 $\mu$m thick copper foil is simply laminated onto the flat front-facing surface of the mirror. Since the band-pass filters have small and complex internal features, commercial electroplating of $\sim$50 $\mu$m thick copper is chosen [14].

As the holey beamsplitter requires dimensional adjustments with its iterative cycle, the script-based CAD drawing software, OpenSCAD [32], is used. Being only 500 $\mu$m thick, this component is too delicate for commercial electroplating; hence, gold leaf gilding is employed [14]. Applying more than one layer of gold leaf causes glue to clump between the holes, causing uneven surfaces. Therefore, only a single layer of gold leaf is gilded onto one side of the holey beamsplitter's 3-D printed skeletal frame.

The 300 $\mu$m separation distance between the square holes is large enough to be FDM 3-D printed (having a 200 $\mu$m diameter nozzle size), while the extrusion speed is sufficiently reduced to prevent mesh breakage. With an FDM 3-D print layer height of 100 $\mu$m, multiple layers were deposited to


**FIGURE 7.** Illustration of the limitation for TRL calibration at the VNA's frequency extension heads for our free-space quasi-optical measurement platform.

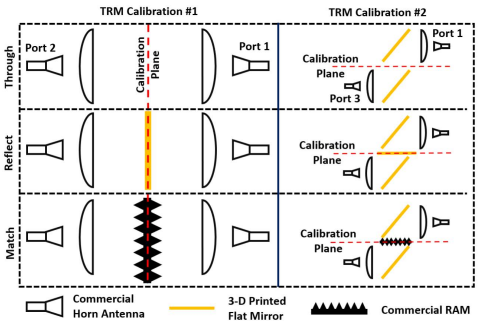


**FIGURE 8.** Illustration of free-space TRM Calibration #1 (left) and #2 (right) for our reconfigurable quasi-optical measurement platform.

give a mesh thickness of approximately 500 $\mu$m; this provides sufficient mechanical rigidity for our application. A low viscosity acrylic glue is applied with a very fine brush to one surface of the 3-D printed part; this is allowed to partially-dry before the gold leaf is gilded. The only design variable left is the physical size of the square holes needed to provide an equal power split, as discussed in Section IIB.

## IV. COMPONENT MEASUREMENT

All electromagnetic measurements are undertaken at the U.K.'s National Physical Laboratory (NPL), using their Keysight Technologies PNA-X N5247B vector network analyzer (VNA) – with VDI WR-5.1 frequency extension heads [35].

Two different calibration methodologies are needed: Thru-Reflect-Line (TRL) calibration in conventional metal-pipe rectangular waveguide, with reference planes at the VNA frequency extension heads; and Thru-Reflect-Match (TRM) calibration in free space having two reference plane options.

After completing the TRL calibration, commercial Flann Microwave Ltd 20 dBi standard gain rectangular horn antennas are fixed to each port [36]. The antennas, with their interface adapters, are then slotted into the quasi-optical test platform shown in Fig. 4. This set-up still has its calibration reference planes located at the flanges of the frequency extension heads. Therefore, any subsequent measurements will include the adverse effects due to the non-ideal horn antennas, lenses and free-space channel, illustrated in Fig. 7.

To avoid these adverse effects, while isolating the device under test in free-space, TRM calibrations are employed for some of the measurements, which are widely used for free-space material characterization [37]. TRM calibration does not require movement of any components during its

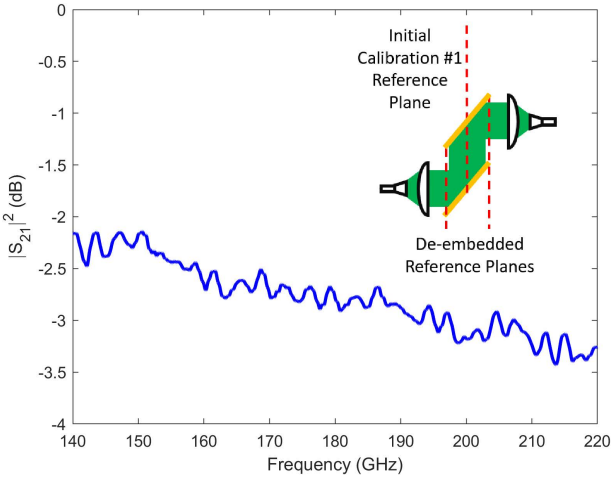


**FIGURE 9.** Measured transmission through two flat mirrors at 45° incidence using TRM Calibration #1 with additional de-embedding of the reference planes (running averaging applied across 3.2 GHz).

calibration process [38], making it ideal for our fixed position test platform. Proprietary software containing an automated TRM algorithm, within the PNA-X, was used to calibrate our 3-D printed test platform using our 3-D printed Thru-Reflect-Match calibration standards.

As shown in Fig. 3, the beamsplitter represents a 3-Port network that requires both transmittance and reflectance measurements. However, since the VNA and its frequency extension heads only support 2-Port testing, two different sets of measurements are required, each having their own calibration. For the transmittance measurements, TRM Calibration #1 is adopted, as illustrated on the left-hand side of Fig. 8. For the reflectance measurements, TRM Calibration #2 is adopted, as illustrated on the right-hand side of Fig. 8. For both calibrations, 3-D printed flat mirrors and commercial pyramidal absorbers (TK Instruments [39]) are used for the Reflect and Match standards, respectively. These calibrations provide an initial common reference plane positioned midway between the lenses.

### A. FLAT MIRROR

Using the quasi-optical test platform shown in Fig. 4, with TRM Calibration #1 shown in Fig. 8, the performance of the flat mirror is evaluated. A pair of identical flat mirrors, at an oblique incidence angle of 45°, creates a thru-line, as illustrated by the insert in Fig. 9. The initial TRM Calibration #1 reference plane is effectively split in two and shifted from the center of the mirrors to their outer edges. As a result, the transmission measurement, in Fig. 9, represents the combined losses from both flat mirrors (e.g., misalignment, ohmic and surface defect-related diffuse reflection scattering) and non-ideal beam collimation exacerbated by excess path lengths between mirrors. It can be seen that a single flat mirror is expected to have an associated loss of 1-2 dB. However, it is important to note that this result only represents a rough pseudo-qualitative estimation of the flat mirror's performance.

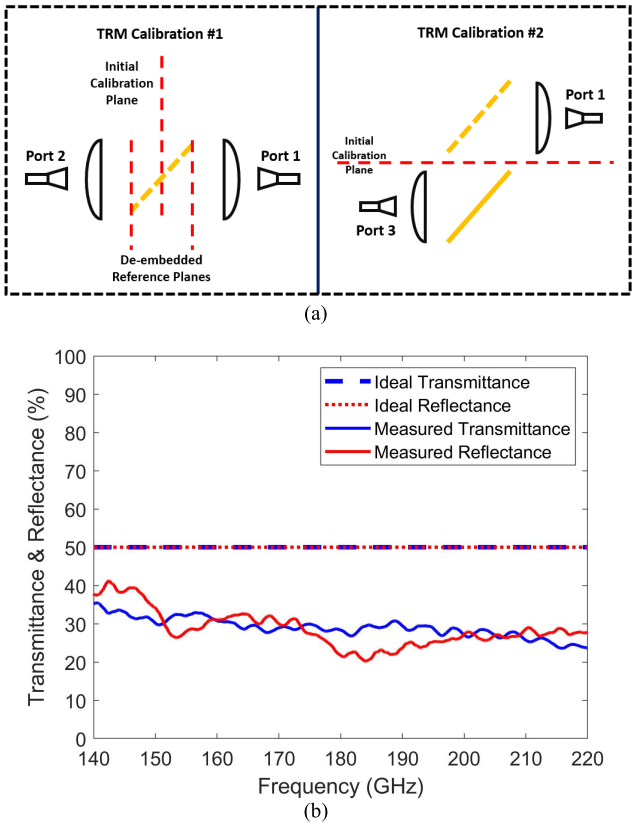


**FIGURE 10.** Holey beamsplitter measurements: (a) illustration of the test set-ups using TRM Calibration #1 (with additional de-embedding of the reference planes) and #2 for measuring transmittance and reflectance, respectively; and (b) measured transmittance and reflectance at 45° incidence (running averaging applied over 3.2 GHz).

**TABLE 3.** Beamsplitter performance comparison.

| Response (%) | Ideal | Commercial Polka Dot (Optical) [16] | 3-D Printed Holey (G-band) |
|---|---|---|---|
| Transmittance, $\mathcal{T}$ | 50 | 40 – 50 | 25 – 35 |
| Reflectance, $\mathcal{R}$ | 50 | 40 – 50 | 25 – 40 |
| Absorptance, $\mathcal{A}$ | 0 | 10 – 20 | 30 – 50 |
| $\lvert\mathcal{T} - \mathcal{R}\rvert$ | 0 | 5 – 10 | 5 – 10 |

### B. HOLEY BEAMSPLITTER

Using the same 3-port quasi-optical test platform, shown in Fig. 4, the 3-D printed holey beamsplitter is now evaluated. The measurement set-up employs both TRM Calibrations #1 and #2, illustrated in Fig. 10(a), for the transmittance and reflectance measurements, respectively, with results shown in Fig. 10(b). With the former, the initial TRM Calibration #1 reference plane is effectively split and shifted from the center of the beamsplitter to its outer edges.

Figure 10 shows that the holey beamsplitter is able to equally divide the incident power; fulfilling our primary objective. The maximum difference between transmittance and reflectance is less than 9%, across G-band. Ideally, absorptance should be 0%. In practice, due to a number of

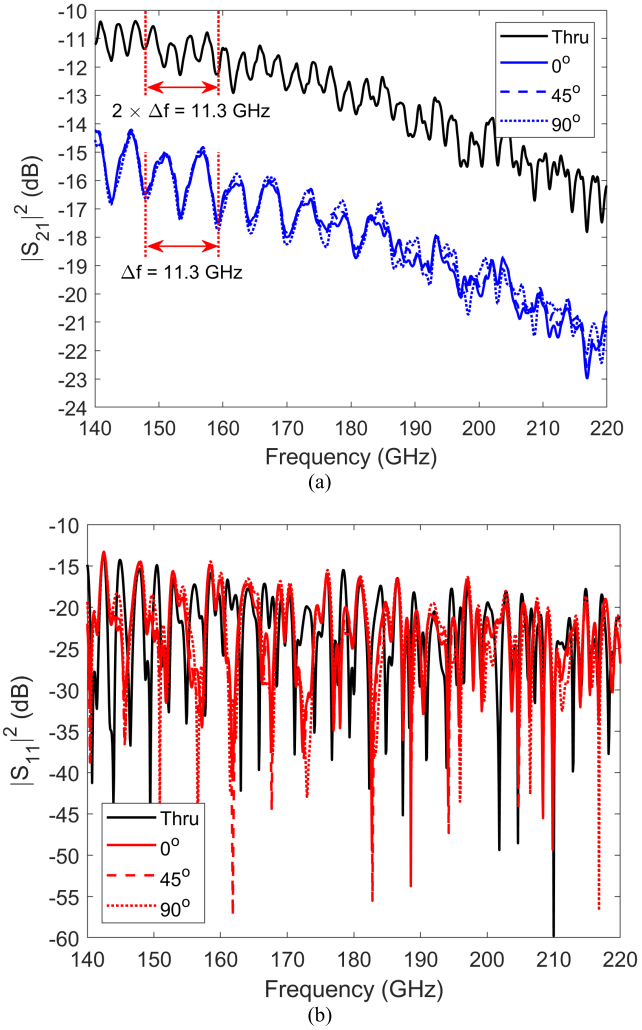


**FIGURE 11.** Holey beamsplitter transmission measurements for different polarizations (transverse angles of rotation) with TRL calibration: (a) transmission; and (b) reflection (no running averaging applied).

factors (e.g., diffraction, diffuse scattering, non-ideal beam collimation and ohmic losses), our holey beamsplitter has approximately 30-50% of absorptance. Table 3 shows the performance of ideal, typical commercial optical and our holey beamsplitters. When compared to the commercial optical polka dot beamsplitter, our millimeter-wave proof-of principle demonstrator has approximately 20-30% more absorptance.

With our vertically-polarized collimated beams, the S-parameters are measured at different transverse angles of rotation, using the 3-D printed polarization test platform, shown in Fig. 5. For this measurement, conventional TRL calibration at the VNA's frequency extension heads is performed. As shown in Fig. 11(a), the beamsplitter has identical transmission responses at three transverse angles of rotation (0°, 45° and 90°); confirming polarization independence.

The normalized transmittance of the beamsplitter at normal incidence, with quasi-optical test fixture, $\mathcal{T}_n$ (dB) $\cong$ $|S_{21}|^2_{Thru}$ (dB) $-$ $|S_{21}|^2$ (dB), where $|S_{21}|^2_{Thru}$ (dB) corresponds

to the transmittance when the beamsplitter is removed. Here, $\mathcal{T}_n$ (dB) $\sim$ 5 dB at 180 GHz, for all three rotation settings; this being comparable to the measured transmittance $\mathcal{T} = 5.5$ dB at 180 GHz, extracted from Fig. 10, at the oblique incidence angle of 45°.

As seen in Fig. 11(b), the reflection responses at all three transverse angles of rotation are also almost identical. It is important to note that, due to the high insertion loss for each lens (>5 dB, discussed in the next sub-section), there is almost no measured difference in reflectance seen in Fig. 11(b), with or without the beamsplitter.

Note that the observed in-band Fabry-Pérot ripples, having frequency period $\Delta f$, correspond to standing-wave reflections between two spatial boundaries that are separated by a theoretical free-space distance $\Delta l = c/\Delta f$. Without the beamsplitter, the extracted value of $\Delta l \cong 53$ mm corresponds to the spatial distance of 55.0 mm between the flat sides of both plano-convex lenses. With the beamsplitter inserted, the extracted value of $\Delta l \cong 26.5$ mm corresponds to the spatial distance of 27.8 mm between the beamsplitter and the flat side of the plano-convex lens. This shows that the metalized side of the beamsplitter is positioned exactly midway between the two plano-convex lenses.

### C. PLANO-CONVEX LENS

Using the 3-D printed test platform shown in Fig. 4, with conventional TRL calibration at the VNA's frequency extension heads, the performance of a lens pair is evaluated. Similar to the arrangement shown in Fig. 7, transmission between two commercial horn antennas, with and without the lenses, is measured. From Fig. 12, it can be seen that adding the lenses provides between 6 to 17 dB of 'gain enhancement'. This clearly shows that the lens is performing as expected. The commercial antenna and 3-D printed lens pair exhibits, *in situ*, approximately 5-8 dB of insertion loss across G-band.

Note that the extracted value of $\Delta l \cong 62.5$ mm corresponds to the spatial distance of 65.0 mm between the flat sides of both plano-convex lenses.

### D. WAVEGUIDE FILTERS

The proposed front-end sub-THz subsystem accommodates up to six channels, each having their own band-pass filter. Measured results for four 5$^{th}$ order prototype BPFs are shown in Fig. 13. Further details of our 3-D printed G-band filters is beyond the scope of this paper and will be published in a separate article.

With reference to IEEE standards [40], the internal aperture dimensions for WM-1295 (G-band) metal-pipe rectangular waveguides are 1,295 $\mu$m × 647.5 $\mu$m. All five cavity resonators support the $TE_{101}$ mode and are coupled together using transverse offset inductive irises. Photographs of a 180 GHz H-plane split-block filter are shown in Fig. 13(a), with a side-view of the upper-half (above) and plan-view of the lower-half (below). The corresponding measured frequency responses for four G-band prototype BPFs are shown in Fig. 13(b). It should be noted that the top-right measurements in Fig. 13(b) correspond to the filter in Fig. 13(a); this filter is employed to demonstrate the final subsystem performance for Ch. #1 (presented in Section V).

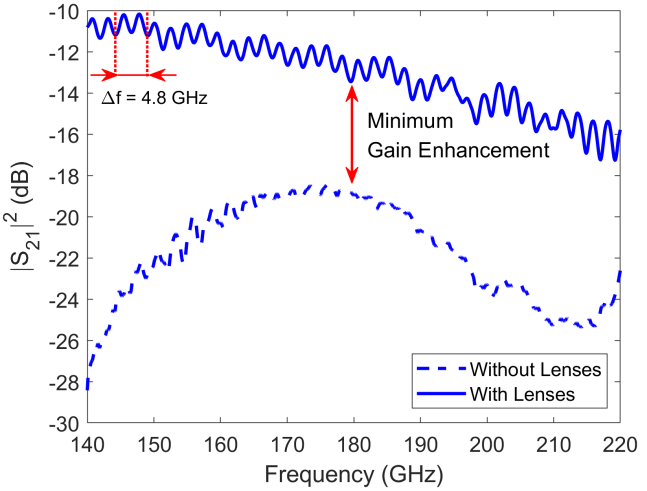


**FIGURE 12.** Plano-convex lens transmission measurements (running averaging applied over 3.2 GHz).

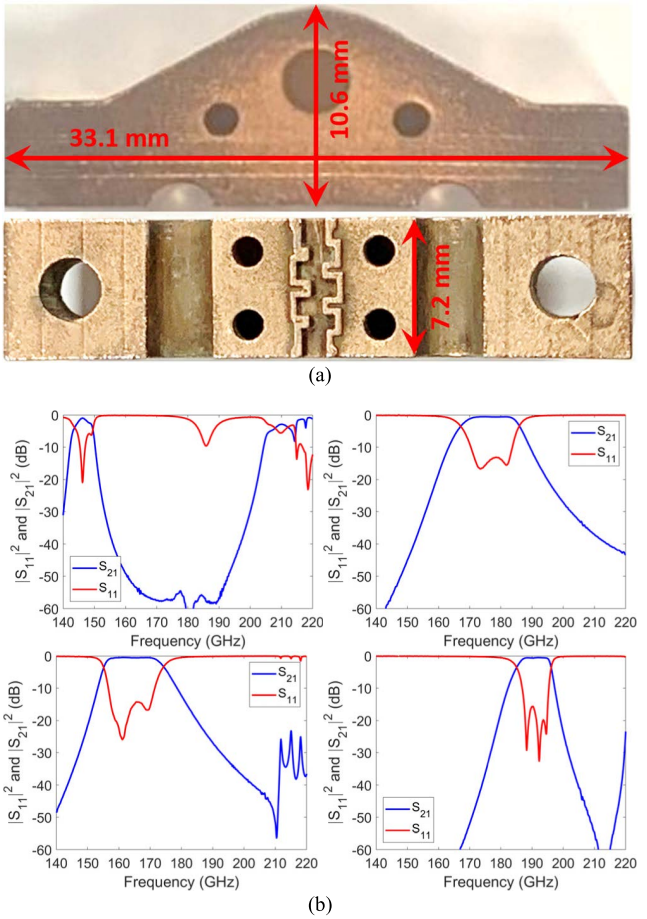


**FIGURE 13.** 3-D printed 5$^{th}$ order band-pass filters: (a) photograph of a typical filter, corresponding to the top-right measurements in (b); and (b) measured frequency performances for four prototype channel filters (no running averaging applied).

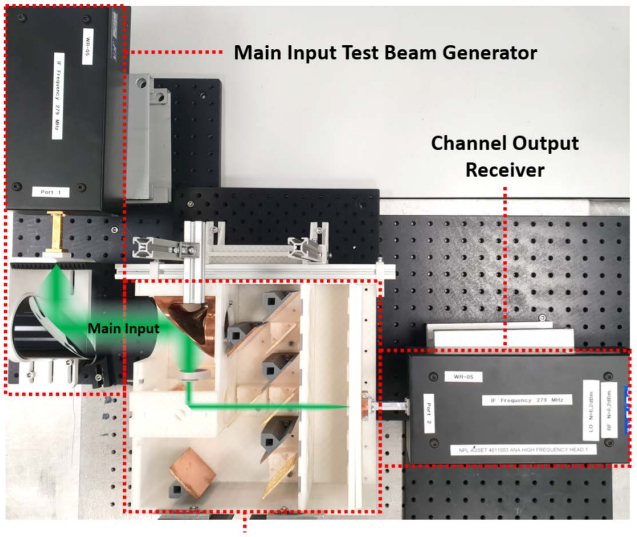


(a)

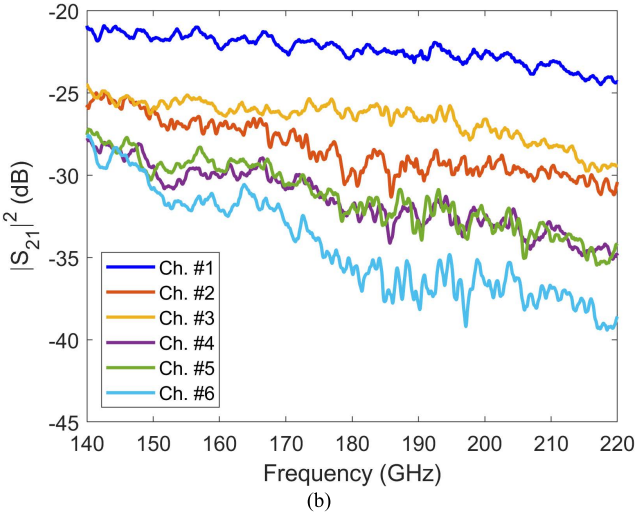


(b)

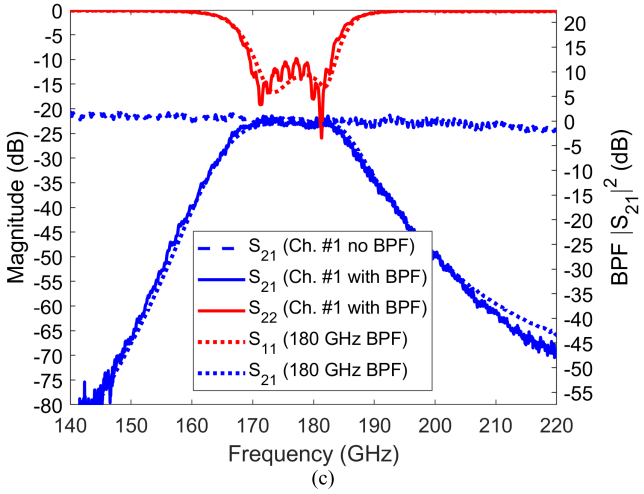


(c)

**FIGURE 14.** Assembled subsystem measurements: (a) photograph of the quasi-optical test set-up; (b) transmission losses for each channel without filters (running averaging applied over 5 GHz); and (c) measured responses for Ch. #1 integrated with the 180 GHz 3-D printed band-pass filter shown in the top-right of Fig. 13(b) (no running averaging applied).

**TABLE 4.** Pseudo-quantitative loss budget analysis at 180 GHz For each element and the complete assembled subsystem (without BPFs).

| Elements (Cumulative) | Estimated Losses (dB) | | | | | |
|---|---|---|---|---|---|---|
| | Ch. #1 | Ch. #2 | Ch. #3 | Ch. #4 | Ch. #5 | Ch. #6 |
| Common Input Stage | 9 | 9 | 9 | 9 | 9 | 9 |
| Removable Flat Mirror | - | - | 1 | 1 | 1 | 1 |
| Flat Mirrors | 1.5 | 3 | - | 1.5 | 1.5 | 3 |
| Beamsplitter Transmissions | 5.5 | - | 11 | 5.5 | 5.5 | - |
| Beamsplitter Reflections | - | 6.6 | - | 6.6 | 6.6 | 13.2 |
| Common Output Stage | 6.5 | 6.5 | 6.5 | 6.5 | 6.5 | 6.5 |
| Non-ideal Collimation | 0.7 | 2.1 | 0.7 | 2.1 | 2.1 | 3.5 |
| Estimated Total Loss | 23 | 27 | 28 | 32 | 32 | 36 |
| Measured Total Loss | 23 | 30 | 27 | 32 | 32 | 36 |

## V. INTEGRATED SUBSYSTEM MEASUREMENTS

With conventional TRL calibration at the VNA's frequency extension heads, the performance of the fully assembled 3-D printed integrated subsystem is evaluated. At Port 1, commercial rectangular horn antenna and 90° OAPM are added to emulate the collimated main input beam [14]; adding an estimated 2 dB of associated losses. Port 2 is connected directly to one of the six output channels, to emulate the channel output receiver. The complete front-end measurement set-up and its results are shown in Fig. 14.

The measured transmission results for the six channels, without their filters, are shown in Fig. 14(b). The lowest transmission loss is observed with Ch. #1, as expected; between 21 and 24 dB across G-band. The highest transmission loss is observed with Ch. #6; between 27 and 40 dB across G-band. Clearly, performance degrades as frequency increases, due to non-ideal beam collimation, which is exacerbated with longer path lengths. With the 180 GHz BPF integrated into Ch. #1, the measured results are shown in Fig. 14(c). With the filter included, despite all possible losses, the subsystem works as expected and exhibits good dynamic range.

Significant computational resources are needed to undertake numerical free-space electromagnetic modeling of individual quasi-optical components. Unfortunately, the lack of such resources prevent us from undertaking rigorous quantitative analysis of the complete integrated system. As a result, it is beyond the scope of this paper to accurately quantify the loss contributions associated with each and every component *in situ*. However, using the measurements in Fig. 14(b) and with information for individual component (from Section IV), it is possible to make a pseudo-quantitative loss budget analysis for the complete subsystem.

An estimated loss for each component type is assigned and their total loss is then compared with that measured for each channel. From this, we speculate that both the flat mirrors and beamsplitters create an additional loss of ~0.7 dB at 180 GHz in their reflected paths, because the beams are not perfectly collimated. This is further compounded by both external and internal misalignments of the quasi-optical components. The results of our preliminary analysis are shown in

Table 4 and Fig. 6(a). With the exception of Ch. #2, it can be seen that there is good agreement between our estimated and measured total losses.

## VI. DISCUSSION AND CONCLUSION

In this paper, we have significantly expanded our previous works on polymer-based 3-D printing for low-cost waveguides and quasi-optical components. Here, we brought together many of the concepts by demonstrating a complete plug and play 6-channel subsystem for operation between 140 to 220 GHz. This sub-THz front-end architecture has successfully integrated 30 individual components: 1× OAPM, 1× plano-concave lens, 1× reconfigurable flat mirror, 5× flat mirrors, 4× beamsplitters, 6× plano-convex lenses, 6× horn antennas and 6× BPFs. It was found that a blend of different 3-D printing technologies and plating methods were needed, depending on the type of component.

In this paper, we introduced bespoke quasi-optical TRM calibrations and measurement schemes with our 3-D printed test platforms. Our 3-D printed flat mirrors demonstrated total losses between 1-2 dB across G-band. The holey beamsplitter was able to divide the input beam into two output beams with equal power. A pair of 3-D printed plano-convex lenses gave up to 17 dB of gain enhancement across G-band. Four BPFs showed good transmission and reflection measured responses. Finally, two test platforms and integrated subsystem housings were all 3-D printed as single pieces, to support plug and play development, while providing sufficient beam alignment accuracy.

Having been able to establish a pseudo-quantitative loss budget for the individual elements, future work on minimizing associated losses can now be investigated. For example, measurements of Ch. #1, having a 180 GHz BPF included, demonstrates a total measured insertion loss of 23 dB for our first proof-of-concept prototype. While this is likely to be too large for most applications, our link budget helps to identify where significant improvements can be made.

Our lenses were made from a relatively lossy 3-D printable dielectric material and so the plano-convex lens exhibited a transmission loss that is >5 dB. Therefore, a 3-D printable dielectric that has a much lower loss tangent will reduce transmission losses; while a greater refractive index will reduce the absorptance due to having a thinner lens, but the impedance-mismatch reflection losses will dominate and increase the net transmission loss. Alternatively, focusing mirrors (e.g., OAPMs) can completely replace the lenses, but this will dramatically increase the size and mass of the assembled subsystem; these and other engineering compromises can be explored in future studies.

Another component worthy of further investigation is the beamsplitter. After considerable investigation, there does not appear to be an obvious 3-D printing alternative to our solution. Nevertheless, with our holey beamsplitter approach, optimization of the internal macroscopic geometrical features (using full-wave electromagnetic simulation software), better material selection and advanced manufacturing techniques, will inevitably reduce its loss characteristics.

One of the major contributors to loss is non-ideal beam collimation and misalignment. Replacing our rectangular horn antenna with a 3-D printed corrugated conical horn antenna will help to preserve the bi-axial symmetry of the beam [14]. Moreover, the manufacturing tolerances associated with our FDM printed housing, plug and play interfaces and adapters can be improved with more advanced, commercial grade 3-D printing technologies.

Diffraction and distortion of beam profiles is not inherent to 3-D printing and so this technology should not have any impact on the design of a future subsystem. With the former, as with any quasi-optical implementation, simply increasing component sizes and/or reducing beamwidths will reduce diffraction losses. With the latter, simply using a better quality 3-D printer will reduce beam distortion.

In conclusion, when compared to using a commercially-machined breadboard and off-the-shelf optical components and their positioners, 3-D printing for prototyping of a complete front-end subsystem offers the important advantage of providing a much more compact solution. In addition, component assembly and alignment are effortless.

This work opens-up new opportunities for rapid prototyping and small-batch production of complete low-cost quasi-optical upper-millimeter-wave subsystems. Indeed, with the continual advancements in all aspects of affordable 3-D printers, and their materials, better resolution and higher performance can be expected in the near future.

## ACKNOWLEDGMENT

The authors would like to thank A. S. Holmes for useful discussions relating to the quasi-optical beamsplitter.

## REFERENCES

[1] P. T. Timbie, J. Grade, D. van der Weide, B. Maffei, and G. Pisano, "Stereolithographed mm-wave corrugated horn antennas," in *Proc. Int. Conf. Infr., Millim., THz Waves (IRMMW-THz)*, Houston, TX, USA, Oct. 2011, pp. 1–3.

[2] A. von Bieren, E. de Rijk, J.-P. Ansermet, and A. Macor, "Monolithic metal-coated plastic components for mm-wave applications," in *Proc. 39th Int. Conf. Infr., Millim., THz waves (IRMMW-THz)*, Tuscon, AZ, USA, Sep. 2014, pp. 1–2.

[3] M. D'Auria, W. J. Otter, J. Hazell, B. T. W. Gillatt, C. Long-Collins, N. M. Ridler, and S. Lucyszyn, "3-D printed metal-pipe rectangular waveguides," *IEEE Trans. Compon., Packag., Manuf. Technol.*, vol. 5, no. 9, pp. 1339–1349, Sep. 2015.

[4] W. J. Otter, N. M. Ridler, H. Yasukochi, K. Soeda, K. Konishi, J. Yumoto, M. Kuwata-Gonokami, and S. Lucyszyn, "3D printed 1.1 THz waveguides," *Electron. Lett.*, vol. 53, no. 7, pp. 471–473, Mar. 2017.

[5] J. Sun, A. Dawood, W. J. Otter, N. M. Ridler, and S. Lucyszyn, "Microwave characterization of low-loss FDM 3-D printed ABS with dielectric-filled metal-pipe rectangular waveguide spectroscopy," *IEEE Access*, vol. 7, pp. 95455–95486, 2019.

[6] E. Marquez-Segura, S.-H. Shin, A. Dawood, N. M. Ridler, and S. Lucyszyn, "Microwave characterization of conductive PLA and its application to a 12 to 18 GHz 3-D printed rotary vane attenuator," *IEEE Access*, vol. 9, pp. 84327–84343, 2021.

[7] B. T. W. Gillatt, M. D'Auria, W. J. Otter, N. M. Ridler, and S. Lucyszyn, "3-D printed variable phase shifter," *IEEE Microw. Wireless Compon. Lett.*, vol. 26, no. 10, pp. 822–824, Oct. 2016.

[8] S.-H. Shin, D. F. Alyasiri, M. D'Auria, W. J. Otter, C. W. Myant, D. Stokes, Z. Tian, N. M. Ridler, and S. Lucyszyn, "Polymer-based 3-D printed Ku-band steerable phased-array antenna subsystem," *IEEE Access*, vol. 7, pp. 106662–106673, 2019.
[9] W. J. Otter and S. Lucyszyn, "Hybrid 3-D-printing technology for tunable THz applications," *Proc. IEEE*, vol. 105, no. 4, pp. 756–767, Apr. 2017.
[10] B. Rohrdantz, C. Rave, and A. F. Jacob, "3D-printed low-cost, low-loss microwave components up to 40 GHz," in *IEEE MTT-S Int. Microw. Symp. Dig.*, San Francisco, CA, USA, May 2016, pp. 1–3.
[11] A. I. Dimitriadis, T. Debogovic, M. Favre, M. Billod, L. Barloggio, J. Ansermet, and E. D. Rijk, "Polymer-based additive manufacturing of high-performance waveguide and antenna components," *Proc. IEEE*, vol. 105, no. 4, pp. 668–676, Apr. 2017.
[12] A. C. Paolella, C. D. Fisher, C. Corey, D. Foster, and D. Silva-Saez, "3-D printed millimeter-wave lens systems at 39 GHz," *IEEE Microw. Wireless Compon. Lett.*, vol. 28, no. 6, pp. 464–466, Jun. 2018.
[13] C. D. Fisher, A. C. Paolella, C. Corey, D. Foster, and D. Silva-Saez, "3-D printed millimeter wave quasi-optical lens system for 60 and 100 GHz applications," in *Proc. IEEE Radio Wireless Symp. (RWS)*, Orlando, FL, USA, Jan. 2019, pp. 1–3.
[14] S.-H. Shin, X. Shang, N. M. Ridler, and S. Lucyszyn, "Polymer-based 3-D printed 140–220 GHz low-cost quasi-optical components and integrated subsystem assembly," *IEEE Access*, vol. 9, pp. 28020–28038, 2021.
[15] Edmund Optics. (2022). *VIS-NIR Polka-Dot Beamsplitters*. Accessed: Mar. 9, 2022. [Online]. Available: https://www.edmundoptics.co.uk/f/vis-nir-polka-dot-beamsplitters/39694/
[16] Thorlabs. (2022). *Polka Dot Beamsplitters*. Accessed: Mar. 9, 2022. [Online]. Available: https://www.thorlabs.com/newgrouppage9.cfm?objectgroup_id=1110
[17] B. Fritz, A. Stephan, P. Walker, C. Brown, A. Nicholas, K. Dymond, S. Budzien, P. Marquis, T. Finne, and K. Wolfram, "Ultraviolet beam splitter characterization for use in a CubeSat optical system," *J. Appl. Remote Sens.*, vol. 13, no. 3, pp. 1–11, Sep. 2019.
[18] H. Yi, S.-W. Qu, K.-B. Ng, C. K. Wong, and C. H. Chan, "Terahertz wavefront control on both sides of the cascaded metasurfaces," *IEEE Trans. Antennas. Propag.*, vol. 66, no. 1, pp. 209–216, Jan. 2018.
[19] X. Zang, H. Gong, Z. Li, J. Xie, Q. Cheng, L. Chen, A. Shkurinov, Y. Zhu, and S. Zhuang, "Metasurface for multi-channel terahertz beam splitters and polarization rotators," *Appl. Phys. Lett.*, vol. 112, no. 17, pp. 1–6, Apr. 2018.
[20] W. Pan, X. Wang, Q. Chen, X. Ren, and Y. Ma, "Terahertz beam splitter based on I-shaped metasurface," *Prog. Electromagn. Res. M*, vol. 90, pp. 27–35, 2020.
[21] J. Li and C. Zhou, "Transmission-type terahertz beam splitter through all-dielectric metasurface," *J. Phys. D, Appl. Phys.*, vol. 54, no. 8, pp. 1–5, Dec. 2020.
[22] J. Li, "Metasurface-assisted reflection-type terahertz beam splitter," *Laser Phys.*, vol. 31, pp. 1–5, Jan. 2021.
[23] B. Ung, C. Fumeaux, H. Lin, B. Fischer, B. Ng, and D. Abbott, "Low-cost ultra-thin broadband terahertz beam-splitter," *Opt. Exp.*, vol. 20, no. 5, pp. 4968–4978, Feb. 2012.
[24] S. Lucyszyn and Y. Zhou, "Characterising room temperature THz metal shielding using the engineering approach," *Prog. Electromagn. Res.*, vol. 103, pp. 17–31, 2010.
[25] Autodesk. (2022). *Fusion 360*. Accessed: Mar. 9, 2022. [Online]. Available: https://www.autodesk.co.uk/products/fusion-360/overview
[26] Raise3D. (2022). *IdeaMaker*. Accessed: Mar. 9, 2022. [Online]. Available: https://www.raise3d.com/ideamaker/
[27] Raise3D. (2022). *Raise Pro2*. Accessed: Mar. 9, 2022. [Online]. Available: https://www.raise3d.com/pro2/
[28] Formlabs. (2022). *PreForm*. Accessed: Mar. 9, 2022. [Online]. Available: https://formlabs.com/uk/software/
[29] Formlabs. (2022). *Form 3*. Accessed: Mar. 9, 2022. [Online]. Available: https://formlabs.com/uk/3d-printers/form-3/
[30] Chitubox. (2022). *Chtubox*. Accessed: Mar. 9, 2022. [Online]. Available: https://www.chitubox.com/en
[31] Elegoo. (2022). *Elegoo Mars 2 Pro*. Accessed: Mar. 9, 2022. [Online]. Available: https://www.elegoo.com/products/elegoo-mars-2-pro-mono-lcd-3d-printer
[32] OpenSCAD. (2022). *OpenSCAD*. Accessed: Mar. 9, 2022. [Online]. Available: https://openscad.org/about.html
[33] Simplify3D. (2022). *Simplify3D*. Accessed: Mar. 9, 2022. [Online]. Available: https://www.simplify3d.com/
[34] Prusa Research. (2022). *Prusa MK3*. Accessed: Mar. 9, 2022. [Online]. Available: https://www.prusa3d.com/
[35] N. Shoaib, N. M. Ridler, and M. J. Salter, "Commissioning of the NPL WR-05 waveguide network analyser system for S-parameter measurements from 140 GHz to 220 GHz," Nat. Phys. Lab., Teddington, U.K., NPL Report, TQE 12, Mar. 2015.
[36] *Calibration Certificates RISE Equipment Used for Test Report 2P03617*. Accessed: Mar. 9, 2022. [Online]. Available: https://fccid.io/TA8AKRX10102/Test-Report/Equipment-certificates-4745782/ViewExhibitReport.cfm
[37] I. Rolfes and B. Schiek, "Calibration methods for microwave free space measurements," *Adv. Radio Sci.*, vol. 2, pp. 19–25, May 2005.
[38] N. Gagnon, J. Shaker, P. Berini, L. Roy, and A. Petosa, "Correction and extraction techniques for dielectric constant determination using a Ka-band free-space measurement system," in *Proc. 32nd Eur. Microw. Conf. (EuMA)*, Milan, Italy, Oct. 2002, pp. 1–4.
[39] TK Instruments. *Thomas Keating and QMC Instruments: Space Capabilities*. Accessed: Mar. 9, 2022. [Online]. Available: http://www.terahertz.co.uk/images/tki/brochures/TK_Space_experience_2013-04-16a.pdf
[40] *IEEE Standard for Rectangular Metallic Waveguides and Their Interfaces for Frequencies of 110 GHz and Above—Part 1: Frequency Bands and Waveguide Dimensions*, IEEE Standard 1785.1-2012, 2012.

**SANG-HEE SHIN** (Member, IEEE) was born in Seoul, South Korea, in 1992. He received the M.Eng. degree in aeronautical engineering and the Ph.D. degree in electrical and electronic engineering from Imperial College London, London, U.K., in 2018 and 2022, respectively. He recently joined the Department of Electromagnetic and Electrochemical Technologies, National Physical Laboratory, U.K., as a Higher Research Scientist. His research interests include designing and manufacturing RF and quasi-optical devices for microwave and millimeter-wave applications using additive manufacturing techniques.

**ROSHAN PAYAPULLI** was born in Bengaluru, India, in 1995. He received the M.Eng. degree in electrical and electronic engineering from Imperial College London, London, U.K., in 2018, where he is currently pursuing the Ph.D. degree with the Department of Electrical and Electronic Engineering.

His research interests include designing and manufacturing lightweight and low-cost waveguide components and systems for microwave and millimeter-wave applications using additive manufacturing techniques.

**LIYAN ZHU** received the B.Eng. degree in electronic science and technology from the Huazhong University of Science and Technology (HUST), Wuhan, China, in 2018, and the M.Sc. degree in telecommunications from University College London (UCL), London, U.K., in 2019. He is currently pursuing the Ph.D. degree with the Department of Electrical and Electronic Engineering, Imperial College London, London, U.K. His research interests include design, fabrication, and sensitivity analysis of microwave components using additive manufacturing techniques.

**MANOJ STANLEY** (Member, IEEE) received the Ph.D. degree in electrical engineering from the University of Liverpool, in 2019. After the completion of his Ph.D. degree, he joined the National Physical Laboratory, U.K., as a Higher Research Scientist at the Electromagnetic Technologies Group. He has supported the development of next-generation computing and communications technologies and high-frequency electronics applications. He is currently developing high-frequency metrology capabilities to characterize superconducting quantum integrated circuits at milli-kelvin temperatures. His research interests include design and characterization of devices at RF and terahertz frequencies, RF metrology for quantum computing applications, material, and channel characterization for 5G and beyond communication. He is the Operations Officer at European Microwave Week 2021.

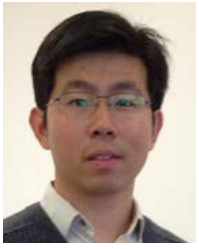

**XIAOBANG SHANG** (Senior Member, IEEE) received the B.Eng. degree (Hons.) in electronics and communication engineering from the University of Birmingham, Birmingham, U.K., in 2008, the B.Eng. degree in electronics and information engineering from the Huazhong University of Science and Technology (HUST), Wuhan, China, in 2008, and the Ph.D. degree in microwave engineering from the University of Birmingham, in 2011. He is currently a Senior Research Scientist with the National Physical Laboratory, Teddington, U.K. He has authored or coauthored more than 90 scientific articles on microwave measurements and microwave circuits. He is a member of the IEEE MTT-3 'Microwave Measurements' Technical Committee and an Associate Editor of the IEEE Microwave and Wireless Components Letters. In 2017, he received both the IEEE Tatsuo Itoh Award and the ARMMS Steve Evans-Pughe Prize.

**NICK M. RIDLER** (Fellow, IEEE) received the B.Sc. degree from King's College London, University of London, London, U.K., in 1981. He is currently the Head of Science at the Electromagnetic and Electrochemical Technologies Department, National Physical Laboratory (NPL), U.K. He is also an NPL Fellow; an Honorary Professor at the University of Glasgow and the University of Liverpool, U.K.; and a Visiting Professor at the University of Kent, the University of Leeds, and the University of Surrey, U.K. He is a Non-Executive Director of LA Techniques Ltd., and a fellow of the Institution of Engineering and Technology (IET) and the Institute of Physics (IOP). He has more than 35 years' experience working in industrial, government and academic research establishments. His research interest includes precision high-frequency electromagnetic measurement (from 1 kHz to 1 THz). He is the General Chair of the European Microwave Week 2021.

**STEPAN LUCYSZYN** (Fellow, IEEE) received the Ph.D. degree in electronic engineering from King's College London, University of London, London, U.K., in 1992, and the D.Sc. (higher doctorate) degree in millimetre-wave and terahertz electronics from Imperial College London, London, in 2010.

He is currently a Professor of millimetre-wave systems with Imperial College London. He co-founded the Imperial College London spin-out company Drayson Wireless Ltd., in 2014. He has coauthored more than 200 articles and 12 book chapters in applied physics and electronic engineering. He was made a fellow of the Institution of Electrical Engineers, U.K., and the Institute of Physics, U.K., in 2005. In 2008, he became a fellow of the Electromagnetics Academy, USA. He was appointed as an IEEE Distinguished Microwave Lecturer, from 2010 to 2013. For his work on 3D printing, Lucyszyn and his team at Imperial College London won Junkosha's inaugural Technology Innovator of the Year Award for the Microwave and Millimeter Wave category, in 2022.